THE JOURNAL OF PHYSICAL CHEMISTRY C

Article

Cite This: J. Phys. Chem. C 2019, 123, 29343−29352

pubs.acs.org/JPCC

Coordination Geometry Engineering in a Doped Disordered Matrix for Tunable Optical Response

Liting Lin,[†,‡] Yunpeng Wang,[§] Bijiao Lan,[†,‡] Jiejie Chen,[†,‡] Shichao Lv,[†,‡] Yujun Zhao,[§] Haohai Yu,[∥] Jianhua Hao,[⊥] Qinyuan Zhang,[†,‡] Zhongmin Yang,[†,‡] Huaijin Zhang,[∥] Jiyang Wang,[∥] Jianrong Qiu,[#] and Shifeng Zhou*[,†,‡]

[†]State Key Laboratory of Luminescent Materials and Devices, School of Materials Science and Engineering, and [§]Department of Physics, South China University of Technology, Guangzhou 510640, China

[‡]Guangdong Provincial Key Laboratory of Fiber Laser Materials and Applied Techniques, Guangdong Engineering Technology Research and Development Center of Special Optical Fiber Materials and Devices, Guangzhou 510640, China

[∥]State Key Laboratory of Crystal Materials and Institute of Crystal Materials, Shandong University, Jinan 250100, China

[⊥]Department of Applied Physics, The Hong Kong Polytechnic University, Kowloon, Hong Kong, China

[#]College of Optical Science and Engineering, Zhejiang University, Hangzhou 310027, China

Supporting Information

ABSTRACT: The controllable incorporation of the dopant element with strictly designed coordination geometry into the target host merits untold scientific and technological potential, yet it has been met with limited success in a disordered matrix. Here, we present a general route for precisely tuning the coordination geometry of the transition metal dopant based on the collaborative element hybridization and crystallization. We experimentally realize the effective switch of tetrahedral and octahedral geometry by using the proof-of-concept Co^{2+} dopant in hybrid glass. We identify that the crystal field stabilization energy should be genetic dominating the above process. The stabilization of high-yield $[CoO_4]^{6-}$ tetrahedron and $[CoF_6]^{4-}$ octahedron in glass enables it to exhibit unique photon−electron−photon effects, including the efficient radiative transition in the blind region of rare earth-doped materials from 2200 to 2600 nm with new record bandwidth (570 nm) and dynamic optical modulation for pulse generation with the duration of 280 ns. The results demonstrate that the proposed strategy provides an effective avenue to construct novel photonic components with multifunctional applications from broadband telecommunication, medical diagnostics, and military countermeasure to trace gas monitoring.

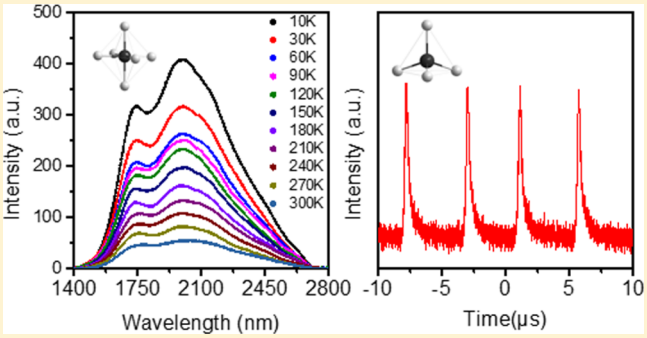

INTRODUCTION

Transition metals are closely related to a variety of fascinating chemical and physical properties including superconductivity, magnetism, multiferroics, catalysis, and luminescence.[1−6] These properties are mainly governed by the coupling manner between the central transition-metal and donor species through the outmost d-electrons. To achieve the desired coupling configuration, the most successful methodology is dedicated to control the coordination geometry around transition-metal centers with a given number of d-electrons. Benefiting from the ordered structural framework of crystalline solids, various types of regular ligand arrangements such as tetrahedral, octahedral, and even square-planar coordination have been accessed in the field of transition-metal chemistry.[1,7,8] In stark contrast, the rational control of the coordination geometry in an amorphous matrix remains a formidable challenge, which has been a long-standing significant issue in condensed matter physics and material science.

Here, we present the evidence that highly efficient switch of coordination geometry around transition-metal dopants can be realized by the collaborative element hybridization and crystallization in nanostructured glass. The element hybridization here means that the elements and structure units are rationally introduced for enhancing the thermodynamic driving force to trigger transition-metal orientation. We have found that this intriguing process helps us to achieve a new structure and energy balance between the central metal and the surrounding ligand and can overcome the widely reported unavoidable chaos of coordination geometry in amorphous materials. As a proof of the concept, it has been attainable to achieve $[CoO_4]^{6-}$ tetrahedron and $[CoF_6]^{4-}$ octahedron geometry with a high ratio in nanostructured glass. These two extreme structure units have gifted the glass with

Received: September 29, 2019
Revised: November 13, 2019
Published: November 16, 2019

DOI: 10.1021/acs.jpcc.9b09195
J. Phys. Chem. C 2019, 123, 29343−29352

unprecedented optical response, including broadband emission and optical pulse generation at the infrared waveband.

EXPERIMENTAL SECTION

Sample Preparation. The samples were prepared by the melt-quenching method. The employed glass systems were designed based on the standard phase diagram, and their composition was optimized by the orthogonal trial and error test. The final systems of $56.5SiO_2-19.5Ga_2O_3-6.5Al_2O_3-7Na_2O-10.5MgO-0.2CoO$ (G), $25KF-25ZnF_2-50SiO_2-0.2CoO$ (KZF), and $50SiO_2-20Al_2O_3-10NaF-20MgF_2-0.2CoO$ (MF) (molar basis) were selected.[9−11] The high purity SiO_2, Ga_2O_3, Al_2O_3, Na_2CO_3, MgO, KF, ZnF_2, NaF, MgF_2, and CoO were used as raw materials. Especially, Na_2O, MgO, Al_2O_3, and NaF were employed as flux and glass network modifiers, which may greatly modify the glass relaxation and crystallization behavior.[12,13] In a typical synthesis procedure, approximate 40 g of raw materials were mixed thoroughly and melted in Pt−Rh crucibles in the temperature ranges from 1450 to 1600 °C for 30 min in air. The homogeneous melts were quenched on the copper plate and pressed with another brass brick immediately to form the rapidly quenched samples. The thermal behaviors of the samples were investigated by using differential thermal analysis (DTA), and the results were used to guide the design of procedure for in situ thermal activation of Ga_2O_3, $KZnF_3$, and MgF_2 crystalline nanoparticles. After heat treatment, the nanostructured samples were cut into pieces and polished for further characterizations.

Optical fibers were fabricated by the unique melt-in-tube strategy. The core glass was polished into cylindrical rods with the diameter of 3.8 mm. The rods with super optical quality were sleeved into cylindrical silica glass tubes (99.999%) with the inner diameter of 4 mm, external diameter of 20 mm, and length of 150 mm. One end of the tube was sealed to form a preform. Finally, this preform assembly was drawn into optical fibers in the fiber-drawing tower at the temperature of 1900 °C. The parameters were optimized based on the in situ feedback system.

Sample Characterization. Thermal behavior analysis was performed on a NETZSCH STA449C differential thermal analyzer with a heating rate of 10 K min^{-1}. The phases of the samples were investigated on a PANalytical X'Pert Pro X-ray diffractometer with Cu Kα radiation at 40 mA and 40 kV (λ = 1.5406 Å). Microstructure and microanalysis of samples were examined through transmission electron microscopy (TEM) on a FEI Tecnai G2 F20 with a field emission gun operated at 200 kV. The topological structure features of the samples were studied on a Renishaw inVia Raman spectrometer. The chemical state and coordination geometry of the dopant were characterized with X-ray absorption spectroscopy (XAS), which was recorded at 1W1B beam line (XAFS station) at the Beijing Synchrotron Radiation Facility. The storage ring energy was operated at 2.5 GeV with a maximum current of about 250 mA. The fabricated samples were measured in the transmission mode using a Si(111) double-crystal monochromator, and the reference samples were recorded in the fluorescence mode using an ionization chamber. The extended X-ray absorption fine structure (EXAFS) data were extracted from the measured absorption spectra by standard methods using the ATHENA module implemented in IFFEFIT software package. The absorption features were measured using a Lambda 900 UV/vis/NIR spectrophotometer. The luminescence properties and the corresponding decay dynamics were studied on an Edinburgh FLS980 spectrometer. The optical fiber was examined by the electron probe micro analysis (EPMA) on a Shimadzu EPMA-1600 electron probe microanalyzer.

Theoretical Simulations. The calculations were performed by using the Vienna Ab initio Simulation Package in the framework of density functional theory.[14,15] The electronic exchange−correlation functional was described by the projector augment wave method with generalized gradient approximation of the Perdew−Burke−Ernzerhof functional.[16] The supercell with 1 × 1 × 1, 3 × 3 × 2, and 3 × 2 × 2 times the primitive unit cells was adopted. The cut-off energy of a plane-wave basis set was set as 520 eV. The meshes of 5 × 5 × 5, 4 × 4 × 6, and 7 × 7 × 7 obtained by the Monkhorst−Pack method were used to sample the Brillouin zone,[17] and all the force criteria is 0.02 eV $Å^{-1}$.

The formation energies of all the possible intrinsic defects were calculated based on the following equation[18,19]

$$\Delta H_f^{(\alpha,q)} = E_D^{(\alpha,q)} - E_P + \sum_i n_i(\Delta\mu_i + \mu_i^{solid}) + q(E_{VBM} + E_F + \Delta V) \quad (1)$$

where q is the charge state of defect α, $E_D^{(\alpha,q)}$ is the total energy of supercells with defect α, E_P is the total energies of supercells containing just the host, n_i is the number of each element, $\Delta\mu_i$ is the atom chemical potential of constitute i referred to its most stable phase with energy μsolid i, E_{VBM} is referenced to the valence-band maximum (VBM) of the defect free system, and E_F is the Fermi level relative to the E_{VBM}. ΔV is a potential alignment correction term used to align the VBM energy in systems with different charged states.[20]

RESULTS AND DISCUSSION

Design and Construction of Material Candidates. We initiated the research in the silica-derived glass system because it has been widely recognized as the most promising platform for developing advanced-generation photonics. Cobalt (Co) species was selected as the porotype of the transition metal, taking into account its interesting multiple physical properties, while unmanageable coordination configuration.[5,21,22] Our design principle is to further seek elements and structure units with enhanced thermodynamic driving force to trigger transition-metal orientation. In the search for the appropriate candidates, we considered that they should be: (1) geometrically matched as much as possible to the desired coordination and (2) potentially favorable for relaxation and crystallization after incorporation into the glass matrix. For the first feature, we are particularly interested in tetrahedral and octahedral coordinations because they potentially endow the transition-metal elements with fascinating properties. For the second feature, we regard the field strength (FS) as the key indicator, and an increase in FS magnitude represents the trend of enhanced relaxation and crystallization. By following these two essential criteria, we conducted a systematic element screening and identified four suitable candidates, that is, Ga, Zn, Mg, and F that simultaneously satisfy the geometric feature (strong tetrahedral or octahedral preference) and crystallization habit (large FS with $FS_{Ga^{3+}}$ = 63.83, $FS_{Zn^{2+}}$ = 27.03 and $FS_{Mg^{2+}}$ = 27.78). F was additionally introduced as the so-called "clustering catalyst" because of its strong network breaking ability. We reasoned that introduction of these elements may

DOI: 10.1021/acs.jpcc.9b09195
J. Phys. Chem. C 2019, 123, 29343−29352

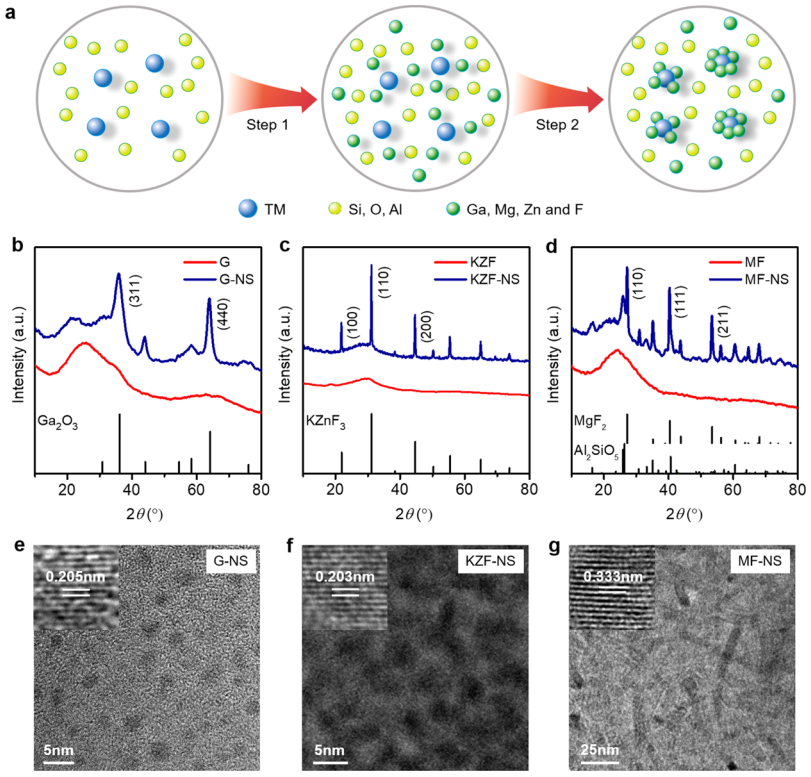

Figure 1. Microstructure evolution after element hybridization and crystallization. (a) Schematic illustration of the element hybridization induced crystallization of glass and transition-metal orientation. Because the raw materials will be melted at high temperature and the chemical bonding will be totally broken, the species involved in the reactions are represented as individual elements. (b–d) XRD patterns of the rapidly quenched and nanostructured samples. Patterns of Ga_2O_3 (JCPDS file number 00-020-0426), $KZnF_3$ (JCPDS file number 01-078-1962), MgF_2 (JCPDS file number 01-072-1150), and Al_2SiO_5 (JCPDS file number 01-083-1566) are also shown. (e–g) TEM images of the nanostructured samples. Insets show the corresponding high-resolution TEM images.

trigger the crystallization of the disordered matrix and transition-metal orientation (Figure 1a).

To validate the proposed design principle, we incorporated Ga^{3+}, $Zn^{2+}/K^{+}/F^{-}$, and Mg^{2+}/F^{-} into the glass matrix. The rapidly quenched samples are denoted as G, KZF, and MF, and the corresponding nanostructured samples after relaxation and crystallization are indicated as G-NS, KZF-NS, and MF-NS, respectively. Nanocrystallization means that the host matrix is still glass phase and dense nanocrystals are in situ precipitated and embedded in the glassy matrix. The glass relaxation and crystallization behavior was studied by using DTA. The inclusion of Ga^{3+}, $Zn^{2+}/K^{+}/F^{-}$, and Mg^{2+}/F^{-} was found to generate prominent exothermic peaks (Figure S1), which stem from the release of cohesive energy during local structure arrangement. Notably, all of the exothermic peaks locate just slightly above the glass transition regions with the characteristic temperatures estimated to be 815, 552, and 745 °C for G, KZF, and MF, respectively. The results indicate the significantly enhanced crystallization tendency when element hybridization occurs. The activation energy of crystallization can experimentally fitted to be 401.46, 201.01, and 410.92 kJ mol^{-1}, respectively (Figure S2). The glass crystallization proceeds in the corresponding exothermic region, and the resultant microstructures were systematically studied. All samples were first examined by X-ray powder diffraction (XRD) (Figure 1b–d) and Raman scattering spectroscopy (Figure S3). The XRD patterns of G-NS, KZF-NS, and MF-NS samples can be well indexed as the spinel phase of Ga_2O_3, perovskite phase of $KZnF_3$, and the combination phases of rutile MgF_2 and sillimanite Al_2SiO_5, respectively. The Raman scattering spectra show several characteristic peaks at 641 cm^{-1} and 766 cm^{-1} for sample G-NS, 580 cm^{-1} for sample KZF-NS, and 293 and 408 cm^{-1} for sample MF-NS, which can be assigned to the regular Ga–O, Zn–F, and Mg–F structure units, respectively. The TEM images (Figure 1e–g) reveal that the uniform nanostructures are dispersed in the glass matrix, with the spherical shape of the Ga_2O_3 particles (~2 nm) and $KZnF_3$ particles (~5 nm), and rodlike morphology of MgF_2 (~3 × 3 × 35 nm). High-resolution TEM images exhibit lattice fringes with the estimated *d*-spacing of 0.205, 0.203, and 0.333 nm, which match well with the lattice spacing in the (400) planes of Ga_2O_3, (200) planes of $KZnF_3$, and (110) planes of MgF_2, respectively. In stark contrast, the amorphous structure of the rapidly quenched samples is maintained because of an extremely high quenching rate (~500 K s^{-1}) during the fabrication process (Figure 1b–d). Taken all together, these results unambiguously suggest the critical role of element hybridization in cultivation of the desired crystallization habit and subsequently, intentional manipulation of the precipitated phases in the disordered matrix.

Experimental Investigation of the Coordination Geometry of Dopant. In addition to the effect on the crystallization process, controllable element hybridization also creates significant changes in the coordination geometry of transition-metal dopant. Steady-state absorption spectroscopy investigation reveals that Co element occupies tetrahedral coordination in the nanostructured sample of G-NS, namely the characteristic absorption at 558, 594, and 646 nm in the

DOI: 10.1021/acs.jpcc.9b09195
J. Phys. Chem. C 2019, 123, 29343–29352

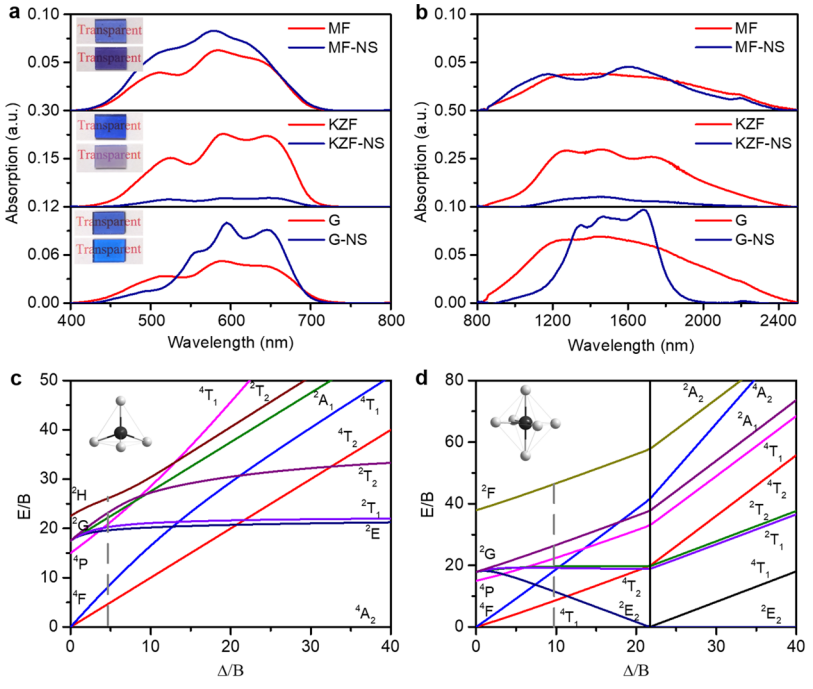

e

	Expt. (cm^{-1})	Fitted (cm^{-1})
Dq	376	-
B	806	-
$^4A_2(^4F)\rightarrow{}^4T_2(^4F)$	-	3749
$^4T_1(^4F)$	6536	6519
$^2E(^2G)$	15479	15808
$^2T_1(^2G)$	-	16359
$^4T_1(^4P)$	16835	16869
$^2A_1(^2G)$	17921	17840
$^2T_2(^2G)$	-	18659
$^2T_2(^2H)$	-	21024

f

	Expt. (cm^{-1})	Fitted (cm^{-1})
Dq	833	-
B	855	-
$^4T_1(^4F)\rightarrow{}^4T_2(^4F)$	7435	7268
$^2E(^2G)$	-	9893
$^4A_2(^4F)$	15385	15553
$^2T_1(^2G)$	-	16392
$^2T_2(^2G)$	16920	16845
$^4T_1(^4P)$	19048	19019
$^2A_1(^2G)$	-	22574
$^2A_2(^2F)$	-	39633

Figure 2. Coordination geometry of Co dopant studied by the spectroscopic method. (a,b) Absorption spectra of the rapidly quenched and nanostructured samples in the visible/infrared waveband region. The insets exhibit the photographs of the fabricated samples. (c,d) Ligand field energy level diagram of tetrahedral and octahedral Co dopant was calculated based on the Tanabe−Sugano theory. The dashed curves indicate the crystal field of Co dopant in G-NS (c) and KZF-NS (d). The insets present the corresponding structure units. (e,f) Comparison of experimentally observed and theoretically simulated energy levels of Co dopant in G-NS (e) and KZF-NS (f).

visible region and broadband bands in the infrared 1000−2000 nm region can be well indexed to the $^4A_2(^4F) \rightarrow {}^2A_1(^2G)$, $^4A_2(^4F) \rightarrow {}^4T_1(^4P)$, $^4A_2(^4F) \rightarrow {}^2E(^2G)$, and $^4A_2(^4F) \rightarrow {}^4T_1(^4F)$ transitions of tetrahedral Co^{2+}, respectively (Figure 2a,b).[23] Interestingly, Co element switches to octahedral coordination in nanostructured KZF-NS system: the finger-print absorption at 525, 591, and 650 nm in the visible region and 1345 nm in the infrared region correspond exactly to the $^4T_1(^4F) \rightarrow {}^4T_1(^4P)$, $^4T_1(^4F) \rightarrow {}^2T_2(^2G)$, $^4T_1(^4F) \rightarrow {}^4A_2(^4F)$, and $^4T_1(^4F) \rightarrow {}^4T_2(^4F)$ transitions of octahedral Co^{2+}, respectively (Figure 2a,b).[24] In addition, we compare the absorption spectra of G-NS and KZF-NS samples with the same size (width × length × thickness: 8 mm × 5 mm × 1.5 mm) and same dopant concentration (Figure S4). As shown in Figure S4, the intensity of Co absorption in tetrahedral symmetry (G-NS) is larger than in octahedral symmetry (KZF-NS). In contrast, the absorption features of Co element in nanostructured MF-NS and all of the rapidly quenched samples cannot be solely correlated with a specific ligand, indicating their chaos in the coordination geometry around Co dopant. We further performed calculations on the electronic transitions of regular tetrahedral and octahedral Co dopant based on the Tanabe−Sugano theory, and the corresponding energy level configurations are sketched (Figure 2c,d).[25] The observed characteristic absorption peaks and the calculated energy levels are compared in Figure 2e,f. It can be found that the theoretical predications are in perfect accord with the experimentally observed spectral features, suggesting the selective incorporation of Co dopant into tetrahedral and octahedral positions in nanostructured G-NS and KZF-NS samples, respectively.

To gain an insight into the accurate chemical state and coordination geometry of Co dopant, XAS characterization including X-ray absorption near edge structure (XANES) and EXAFS was performed. From the XANES spectrum, the absorption edge energy can be calculated and used to distinguish the chemical state of the targeted species. Figure 3a exhibits the XANES spectra of the rapidly quenched and nanostructured samples. The XANES spectra of the rapidly quenched samples resemble each other, and a representative XANES curve is presented here. It can be found that the absorption edge position of all of the fabricated samples is

DOI: 10.1021/acs.jpcc.9b09195
J. Phys. Chem. C 2019, 123, 29343−29352

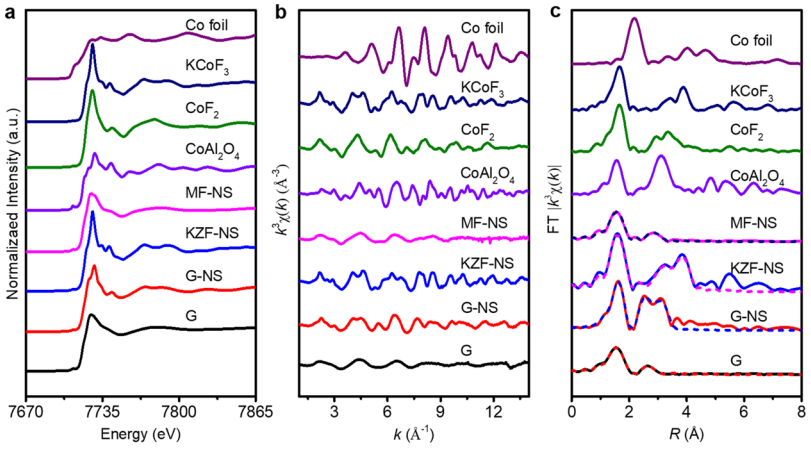

d

Sample	Bound type	R (Å)	N	σ² (Å²*10³)
G	Co–O	1.99 ± 0.03	4.0 ± 0.8	8.6 ± 1.7
	Co–Co	2.86 ± 0.03	0.5 ± 0.1	8.0 ± 1.6
G-NS	Co–O	2.05± 0.03	4.5± 0.9	6.2± 1.2
	Co–Ga	2.92± 0.03	4.9± 1.0	13.2± 2.6
	Co–Ga	3.43± 0.03	9.4± 1.9	14.0± 2.8
KZF-NS	Co–F	2.02± 0.03	5.6± 1.1	5.9± 1.2
	Co–K	3.58± 0.03	8.3± 1.7	11.3± 2.3
	Co–Zn	4.14± 0.03	12.1± 2.4	9.4± 1.9
M-NS	Co–O	2.00 ± 0.03	3.8 ± 0.8	7.0 ± 1.4
	Co–Co	3.13 ± 0.03	1.1 ± 0.2	9.6 ± 1.9

Figure 3. Chemical state and coordination geometry of Co dopant confirmed by XAS techniques. (a–c) Co K-edge EXAFS spectra (a), k^3-weighted $\chi(k)$-function (b), and Fourier transformed k^3-weighted $\chi(k)$-function (c) of EXAFS spectra for the rapidly quenched and nanostructured G-NS, KZF-NS and MF-NS samples. The standard samples, including Co metal, $KCoF_3$, CoF_2, and $CoAl_2O_4$, are also characterized for comparison. (d) Local structural parameters obtained by the curve fitting of the experimental EXAFS spectra.

identical to those of the $CoAl_2O_4$, CoF_2, and $KCoF_3$ reference samples, and the corresponding energy (E_0) is calculated to be ~7717 eV. In contrast, E_0 of Co-foil is estimated to be ~7709 eV. The results demonstrate that the average chemical state of Co in all of the fabricated samples should be +2, which is well consistent with the spectral data in Figure 2. The EXAFS spectrum, which is resulted from the interference of the photoelectron scattered by surrounding atoms, can indicate the chemical coordination environment of the central atom. Figure 3b,c shows the k^3 weighted EXAFS signals and Fourier transform modulus of the Co dopant in nanostructured G-NS, KZF-NS, MF-NS, and various reference samples. The results reveal that the EXAFS signals of Co element in nanostructured MF-NS and all of the rapidly quenched samples are nearly identical to each other and characterized by the single low-frequency oscillation with weak intensity and small amplitude, indicating high distortion of the first coordination around Co dopant. Significantly, the EXAFS signals of Co dopant in nanostructured G-NS and KZF-NS samples exhibit multiple oscillation modes and intermediate-range fingerprint scattering, suggesting the ordered framework around Co dopant.

The coordination geometry reproduction was performed by fitting the Fourier transform of Co K-edge EXAFS spectra of the rapidly quenched and nanostructured G-NS, KZF-NS, and MF-NS samples. The fitting parameters, including the interatomic distance R, the coordination number N, and the Debye–Waller factor value σ^2, are summarized in Figure 3d. The rapidly quenched sample and nanostructured MF-NS exhibit similar small Co–O distance (~2 Å) and rather low coordination number of Co (~4), indicating the disordered geometry of Co dopant in these two samples. For nanostructured G-NS, the reproduced structure unit is $[CoO_4]^{6-}$ tetrahedron with the interatomic distance of first, second, and third shells fitted to be 2.05, 2.92, and 3.43 Å, which are well consistent with the Co–O, Co–Ga, and Co–Ga bonding, respectively. In the case of nanostructured KZF-NS, the simulated structure can be well indexed to the $[CoF_6]^{4-}$ octahedron. The fitted characteristic bonding with the length of 2.02, 3.58, and 4.14 Å is associated with Co–F, Co–K, and Co–Zn coordination shells, respectively; the corresponding coordination number of the first shell around Co dopant is close to 6. Hence, these fitted results collaboratively demonstrate the implement in building the $[CoO_4]^{6-}$ tetrahedron and $[CoF_6]^{4-}$ octahedron geometry in the designed nanostructured glass.

Theoretical Simulation of the Coordination Geometry of Dopant. Another key issue left open is the physical mechanism for the observed hybridization induced coordination geometry switching. In our cases, the structure relaxation in nanostructured glass was fully processed, and it can be anticipated that the principle of lowest crystal field stabilization should dominate the event. To shed more details on it, we performed first-principle quantum mechanical calculations on the stabilization energy of Co dopant in regular $(Ga_2O_3)_x$, $(MgF_2)_x$, and $(KZnF_3)_x$ clusters (Figure 4a–d). For Co dopant in $(Ga_2O_3)_x$, two distinct sites, four-fold (A), and six-fold (B), as indicated in Figure 4a, can be potentially occupied. In order to avoid the formation of competing secondary phases, the chemical potential was restrained to a reasonable range in the theoretical calculations. Significantly, the calculated formation energy of Co dopant in the four-fold (A) site is estimated to be only three-fifths of that in six-fold (B) position, demonstrating that Ga hybridization is highly beneficial for formatting $[CoO_4]^{6-}$ tetrahedron in sample G-NS (Figure 4c). In the

DOI: 10.1021/acs.jpcc.9b09195
J. Phys. Chem. C 2019, 123, 29343–29352

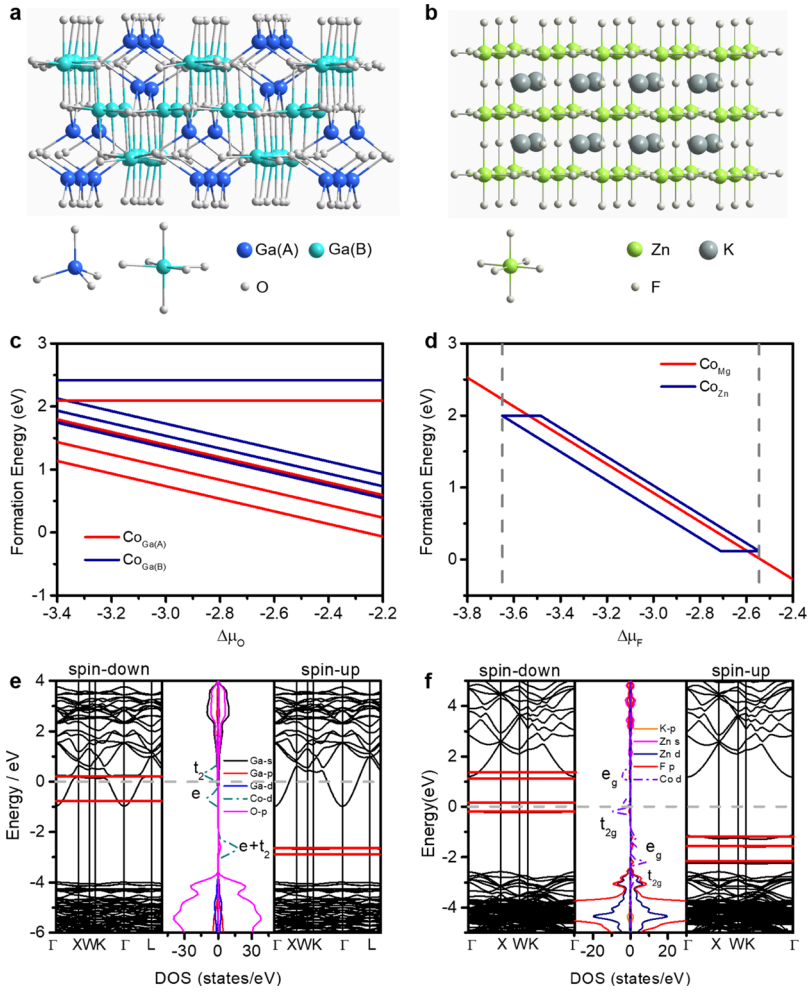

Figure 4. Theoretical investigation on the physical mechanism of coordination geometry switching. (a,b) The structure model of regular $(Ga_2O_3)_x$ (a) and $(KZnF_3)_x$ (b) clusters derived from spinel and perovskite structures. (c,d) Calculated formation energy for the selective incorporation of Co dopant into Ga (c), Mg, and Zn (d) lattice positions. (e,f) Computed electronic band dispersion and PDOS of Ga_2O_3: Co (e) and $KZnF_3$: Co (f).

case of $(MgF_2)_x$ and $(KZnF_3)_x$, it is difficult to directly compare the stability of Co_{Zn} with Co_{Mg} because of the chemical potentials of different elements involved. Fortunately, there is a chemical potential balance between $\Delta\mu_K$ and $\Delta\mu_F$ in $KZnF_3$, so we can analyze the stability of Co_{Zn} and Co_{Mg} with reference to $\Delta\mu_F$. The calculations suggest that only six-fold site is available for Co dopant and the Gibbs free energy for its incorporation into $[ZnF_6]^{4-}$ is generally smaller compared with that in $[MgF_6]^{4-}$ units (Figure 4d), indicating the obvious promotion effect of Zn/K/F hybridization on the creation of $[CoF_6]^{4-}$ octahedron. The significant implication of the above calculation results is that the crystal field stabilization energy should be genetic dominating the final coordination geometry and element hybridization provide an effective avenue for rationally manipulating it.

The electronic structure and the partial densities of states (PDOS) of Co dopant in $(Ga_2O_3)_x$ and $(KZnF_3)_x$ are computed and shown in Figure 4e,f. It can be clearly observed that the Co dopant introduces additional electronic levels into the band gap of both $(Ga_2O_3)_x$ and $(KZnF_3)_x$. The PDOS indicates that these impurity levels stem from Co 3d orbitals, and the corresponding bands exhibit great splitting, suggesting the strong interaction between Co ions and the host units. The simulated single-particle splitting in t_2/t_{2g} and e/e_g orbitals of Co dopant is qualitatively consistent with its tetrahedral or octahedral surrounding obtained via substituting Ga(A) or Zn ion position, respectively (Figure 4a,b). Notably, the calculated energy difference between t_2/t_{2g} and e/e_g states are estimated to be 0.37 and 1.04 eV for Co dopant in $(Ga_2O_3)_x$ and $(KZnF_3)_x$, respectively. The values are in accordance with the experimental values of 0.47 and 1.03 eV, which are estimated directly from the spectroscopic measurements in Figure 2.

Construction of Optical Fibers. In addition to the bulk nanostructured glass, we also attempted to construct optical fibers. According to the DTA analysis (Figure S1), the designed glass is a metastable hybrid system which exhibits great crystallization tendency. To well prevent it, the fiber drawing was processed under low-viscosity conditions and with relatively high speed to keep away from the overlapping region of the nucleation and growth curves. Based on a thorough optimization of various parameters, the fiber with 100 m length can be fabricated within ~7 and 5 min for the sample G and KZF. The constructed optical fibers exhibit superior light-guiding properties which are benefited from the formation of perfect core−clad configuration (Figure 5). It can be confirmed by the element mapping analysis which indicates that the hybridization elements (e.g., Ga and Zn/K/F) and

DOI: 10.1021/acs.jpcc.9b09195
J. Phys. Chem. C 2019, 123, 29343−29352

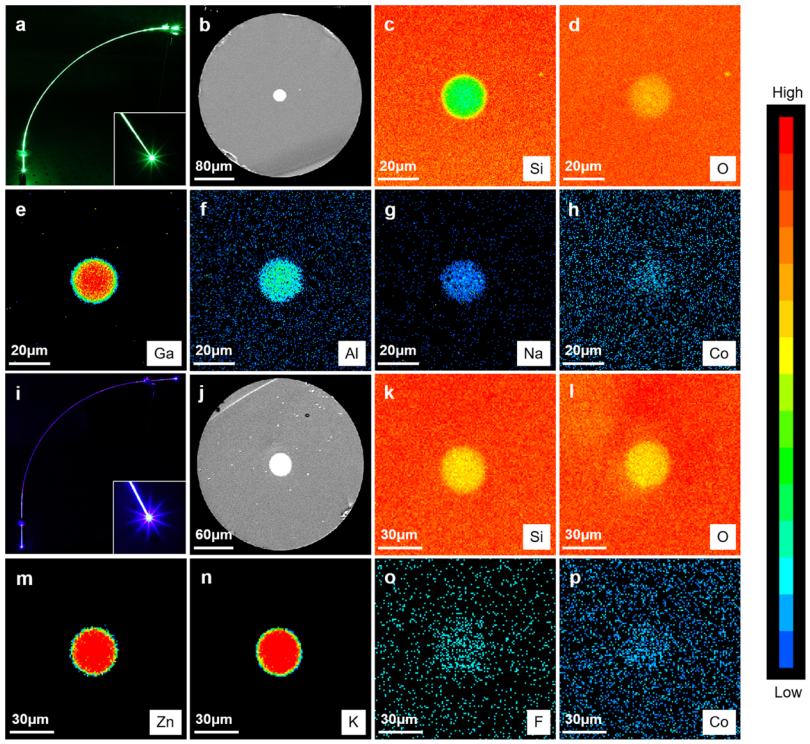

Figure 5. Construction of optical fibers. (a–p) Photographs, scanning electron microscope image, and element mapping analysis of sample G (a–h) and KZF (i–p).

active dopant (Co) are homogeneously distributed in the core region (Figures 5 and S5).

Coordination Geometry Engineering for Novel Photon–Electron–Photon Conversion Process. The success in the engineering of the coordination geometry of transition-metal elements in the disorder system provides a unique opportunity for bringing about novel photon–electron–photon conversion process. For example, a careful examination on the strong energy splitting and the resultant rich energy level configuration (Figure 6a,b) suggests that the small energy-gap between $^4T_1(^4F)$ and $^4T_2(^4F)$ levels in $[CoF_6]^{4-}$ octahedron may potentially support the radiative transition in the near-/mid-infrared waveband region. To verify it, we pumped the electrons in the $^4T_1(^4F)$ ground state to the $^4T_1(^4P)$ excited state by using 532 nm photons and monitored the radiation in the infrared region (Figure 6c) in sample KZF-NS. Encouragingly, intense broadband luminescence covering the wavelength region from 1400 to 2800 nm can be detected, and it should be originated from the $^4T_2(^4F) \rightarrow {}^4T_1(^4F)$ transition after nonrelaxation transition of electrons from the $^4T_1(^4P)$ level (Figure 6d). This optical phenomenon is exciting because to the best of our knowledge, it is the first time to report the near-/mid-infrared luminescence in Co doped photonic glass. The bandwidth, which is represented as the full width at half-maximum (fwhm), is estimated to be 570 nm, with a new record compared with the conventional rare-earth doped active materials.[26] The temperature dependent luminescence from 10 to 300 K indicates that the spectroscopic profile is highly stable and the strong mid-infrared luminescence can be clearly observed at room temperature. The luminescence decay dynamics exhibit nonexponential characteristics at each temperature, and the decay lifetime varies from 394 to 54 μs with change of the temperature. According to the above spectral feature, the stimulated emission cross section σ, which is recognized as the critical physical parameter of functional light source, can be calculated by the Füchtbauer–Ladenburg equation[27]

$$\sigma = \frac{\lambda_0{}^2 \eta}{4c\pi n^2 \tau} \times \left(\frac{\ln 2}{\pi}\right)^{1/2} \times \frac{1}{\Delta\nu_{1/2}} \quad (2)$$

where λ_0 is the central wavelength in the band, η is the internal quantum efficiency that can be defined as τ_{300K}/τ_{5K}, c is the velocity of light, n is the host refractive index, τ is the emission lifetime, and $\Delta\nu_{1/2}$ is the fwhm of the emission. The decay lifetime was fitted to a parabolic function and extrapolated to 0 K. From this extrapolation, the lifetime at 5 K was estimated to be about 394 μs. Based on the above relation, we can obtain $\sigma = 4.17 \times 10^{-20}$ cm^2, with $\lambda_0 = 2040$ nm, $\eta = 0.137$, $n = 1.466$, $\tau = 54$ μs, and $\Delta\nu_{1/2} = 1467$ cm^{-1}. The σ of KZF-NS is higher than that of the $^5I_7 \rightarrow {}^5I_8$ transition of Ho^{3+} doped photonic glass (9.52×10^{-21} cm^2).[28] Furthermore, as the figure of merit for valuation of active materials, the product of σ and τ ($\sigma\tau$) at 300 K was calculated to be 2.2×10^{-24} cm^2·s, which is larger than that of Al_2O_3:Ti^{3+} (1.4×10^{-24} cm^2·s).[29] The above results demonstrate that the present Co doped photonic glass can provide high amplification gain and low laser oscillation threshold in the near-/mid-infrared waveband. More importantly, the achieved radiative transition bridges the near-infrared and mid-infrared wavebands and also covers the blind region of commercial rare-earth activated photonic glass and fiber from 2200 to 2600 nm where no active material is available (Figure S6), pointing to promising applications in the field of medical diagnostics, military countermeasure, and trace gas monitoring.[30−32]

The achievement of coordination geometry with high level of uniformity further prompts us to consider the photonic glass as a smart modulator for pulse laser generation. In this case,

DOI: 10.1021/acs.jpcc.9b09195
J. Phys. Chem. C 2019, 123, 29343−29352

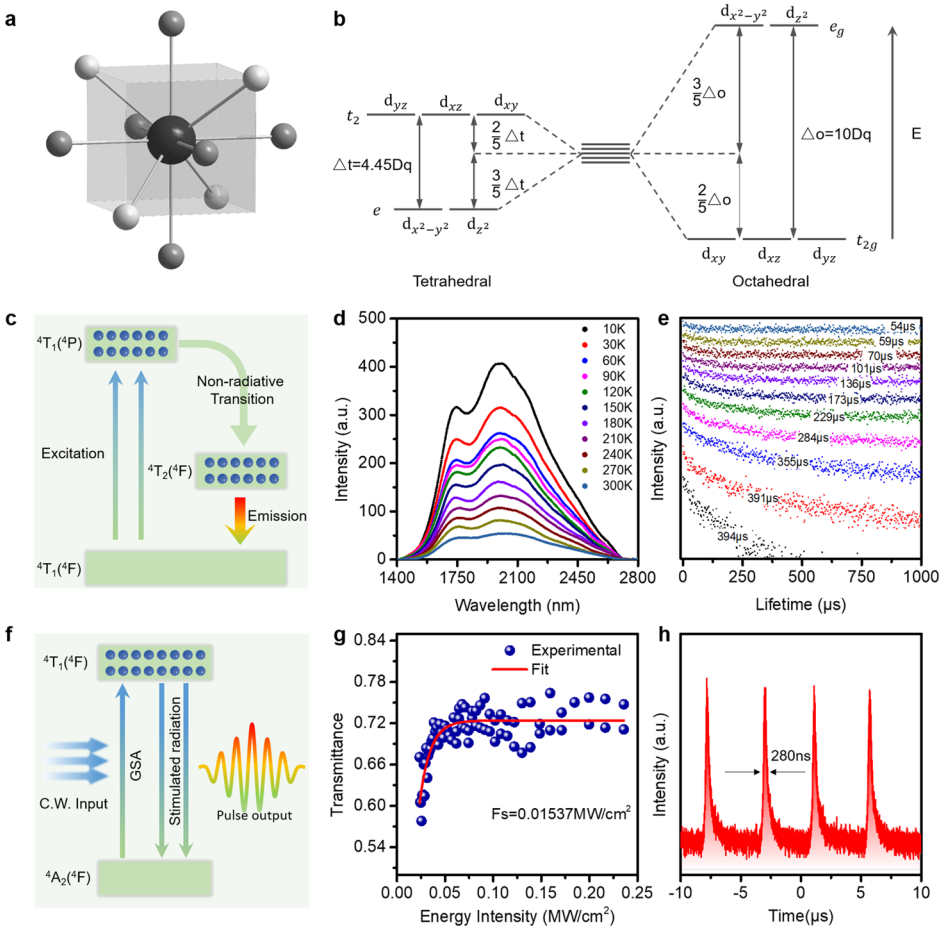

Figure 6. Coordination geometry engineering for near-/mid-infrared luminescence and optical modulation. (a,b) Schematic drawings illustrating the coordination geometry switch (a) and energy level splitting change (b) of Co dopant. (c–e) Proposed electronic transition mechanism (c), near-/mid-infrared luminescence (d), and decay curves (e) from 10 to 300 K in Co-doped photonic glass under excitation with 532 nm photons. (f–h) Proposed electronic transition mechanism (f), dynamic optical absorption (g), and the achieved laser pulse (h) in Co-doped photonic glass.

the energy level with superior capability for management of the dynamic energy storage and its controllable release is critical. The theoretical analysis on the energy level configuration indicates that the energy level pairs of $^4T_1(^4F)$ and $^4A_2(^4F)$ in nanostructured G-NS may satisfy this requirement because they can potentially offer high absorption cross section, weak excited-state absorption, and fast energy recovery time (Figure 6f). To prove the proposed concept, the nonlinear optical response corresponding to these two levels was investigated by the *Z*-scan method, and it can be represented by the internal power-dependent transmittance (Figure 6g). A femtosecond (400 fs) Er^{3+}: glass fiber laser with a repetition rate of 43 MHz and a central wavelength of 1550 nm was used in the experiment. The result clearly shows that the optical transmission increases with the incident energy intensity and reaches to saturation at ~0.05 MW cm^{-2}. Furthermore, the process can be well fitted by using the saturable model[33]

$$T = 1 - T_s \times \exp\left(\frac{-I}{I_{sat}}\right) - T_{ns} \quad (3)$$

where T_s is the modulation depth, T_{ns} is the nonsaturable loss, I is the input peak intensity, and I_{sat} stands the saturation intensity. The corresponding parameters of T_s, T_{ns}, and I_{sat} are estimated to be 64.0%, 26.8%, and 0.01 MW cm^{-2}, respectively. The above fitting results firmly demonstrate the occurrence of the expected dynamic energy storage and release. As the input laser power increases, the electrons in the $^4A_2(^4F)$ energy level are excited into $^4T_1(^4F)$ energy level. This produces a population inversion, and some energy is stored in the G-NS sample. At sufficiently high incident energy intensity, the stored energy will reach a maximum level and the sample subsequently saturates, finally leading to the pulse generation through the electron "avalanche" process. The attractive photon management function further invites us to build a novel pulse laser device. Significantly, the pulsed laser can be realized, and the repetition rate was estimated to be about 200 kHz (Figure 6h). In stark contrast, no pulse can be detected in the rapidly quenched sample, mainly due to the serious unexpected energy loss caused by transition-metal element with irregular coordination geometry. The pulse duration was calculated to be 280 ns which can be further improved when optimizing the optical setup. Moreover, the generated pulse trace is highly stable, and no appreciable degradation can be observed even after keeping for two years, demonstrating its great potential for future all-fiber integration.

CONCLUSIONS

The proposed coordination geometry engineering strategy provides an excellent platform for transition-metal doping studies in the disordered matrix. It possesses the distinct features including (i) generality, (ii) controllability, and (iii)

DOI: 10.1021/acs.jpcc.9b09195
J. Phys. Chem. C 2019, 123, 29343−29352

scalability. The avenue can be applied to switch the coordination geometry of a wide range of transition-metal dopants (e.g., Mn^{2+}), and the configuration of $[MnO_4]^{6-}$ tetrahedron (Figure S7) can be achieved at a high yield level. The coordination geometry engineering strictly relies on the selected hybridized elements and crystallization conditions. Thus, precise control over the parameters (codopants, crystallization temperature, and duration) effectively tunes the types of coordination geometry, their relative ratio and the spatial distribution. The protocol with easily tunable fabrication parameters is suitable for large-scale manufacturing of material candidates with a wide range physical size. For example, in addition to the micrometer-size fiber with high production speed of ~15 m min^{-1}, the bulk photonic glass with the size of 100 mm × 100 mm × 3 mm (width × length × thickness) has also been successfully fabricated in the laboratory. Moreover, the strategy facilitates to engineer d-electrons dominant strong correlations between electrons, spins, and lattices, and the resultant functional characteristics such as magnetic, optical, electric, and catalytic properties, thus potentially leading to broad technological applications.[34−38]

■ ASSOCIATED CONTENT

Supporting Information

The Supporting Information is available free of charge at https://pubs.acs.org/doi/10.1021/acs.jpcc.9b09195.

Differential scanning calorimetry curves of samples, plots of $\ln(T_c^2/\phi)$ versus $1000/T_c$ for samples, Raman spectra of the rapidly quenched and nanostructured samples, absorption spectra of G-NS and KZF-NS samples, scanning electron microscopy image and elemental profiles of cross section, fluorescence spectra of Co-doped KZF-NS sample and rare-earth doped aluminosilicate glass, and coordination geometry engineering in Mn-doped glass (PDF)

■ AUTHOR INFORMATION

Corresponding Author

*E-mail: zhoushifeng@scut.edu.cn. Phone: +86-20-87113646. Fax: +86-20-87114204.

ORCID

Yujun Zhao: 0000-0002-6923-1099
Haohai Yu: 0000-0002-2295-1400
Qinyuan Zhang: 0000-0001-6544-4735
Shifeng Zhou: 0000-0003-4609-763X

Notes

The authors declare no competing financial interest.

■ ACKNOWLEDGMENTS

The authors gratefully acknowledge the financial support from the National Key R&D Program of China (2018YFB1107200), the National Science Fund for Excellent Young Scholars of China (51622206), the National Natural Science Foundation of China (51872095, 51972113), the Local Innovative and Research Teams Project of Guangdong Pearl River Talents Program (2017BT01X137), the Tip-Top Scientific and Technological Innovative Youth Talents of Guangdong Special Support Program (2015TQ01C362), and the Key Program of Guangzhou Scientific Research Special Project (201904020013).

■ REFERENCES

(1) Tsujimoto, Y.; Tassel, C.; Hayashi, N.; Watanabe, T.; Kageyama, H.; Yoshimura, K.; Takano, M.; Ceretti, M.; Ritter, C.; Paulus, W. Infinite-layer iron oxide with a square-planar coordination. *Nature* **2007**, *450*, 1062−1065.

(2) Takahashi, H.; Igawa, K.; Arii, K.; Kamihara, Y.; Hirano, M.; Hosono, H. Superconductivity at 43 K in an iron-based layered compound $LaO_{1-x}F_xFeAs$. *Nature* **2008**, *453*, 376−378.

(3) Maldiney, T.; Bessière, A.; Seguin, J.; Teston, E.; Sharma, S. K.; Viana, B.; Bos, A. J. J.; Dorenbos, P.; Bessodes, M.; Gourier, D.; et al. The in vivo activation of persistent nanophosphors for optical imaging of vascularization, tumours and grafted cells. *Nat. Mater.* **2014**, *13*, 418−426.

(4) Liu, X.; Wang, Y.; Li, X.; Yi, Z.; Deng, R.; Liang, L.; Xie, X.; Loong, D. T. B.; Song, S.; Fan, D.; et al. Binary temporal upconversion codes of Mn^{2+}-activated nanoparticles for multilevel anti-counterfeiting. *Nat. Commun.* **2017**, *8*, 899.

(5) Lu, N.; Zhang, P.; Zhang, Q.; Qiao, R.; He, Q.; Li, H.-B.; Wang, Y.; Guo, J.; Zhang, D.; Duan, Z.; et al. Electric-field control of tri-state phase transformation with a selective dual-ion switch. *Nature* **2017**, *546*, 124−128.

(6) Ma, J.; Ma, J.; Zhang, Q.; Peng, R.; Wang, J.; Liu, C.; Wang, M.; Li, N.; Chen, M.; Cheng, X.; et al. Controllable conductive readout in self-assembled, topologically confined ferroelectric domain walls. *Nat. Nanotechnol.* **2018**, *13*, 947−952.

(7) Li, J.; Medina, E. A.; Stalick, J. K.; Sleight, A. W.; Subramanian, M. A. Colored oxides with hibonite structure: a potential route to non-cobalt blue pigments. *Prog. Solid State Chem.* **2016**, *44*, 107−122.

(8) Kan, D.; Aso, R.; Sato, R.; Haruta, M.; Kurata, H.; Shimakawa, Y. Tuning magnetic anisotropy by interfacially engineering the oxygen coordination environment in a transition metal oxide. *Nat. Mater.* **2016**, *15*, 432−437.

(9) Zhou, S.; Li, C.; Yang, G.; Bi, G.; Xu, B.; Hong, Z.; Miura, K.; Hirao, K.; Qiu, J. Self-limited nanocrystallization-mediated activation of semiconductor nanocrystal in an amorphous solid. *Adv. Funct. Mater.* **2013**, *23*, 5436−5443.

(10) Lin, C.; Bocker, C.; Rüssel, C. Nanocrystallization in oxyfluoride glasses controlled by amorphous phase separation. *Nano Lett.* **2015**, *15*, 6764−6769.

(11) Qiao, X.; Luo, Q.; Fan, X.; Wang, M. Local vibration around rare earth ions in alkaline earth fluorosilicate transparent glass and glass ceramics using Eu^{3+} probe. *J. Rare Earths* **2008**, *26*, 883−888.

(12) Zhang, Y.; Yang, G.; Yue, Y. Calorimetric signature of structural heterogeneity in a ternary silicate glass. *J. Am. Ceram. Soc.* **2013**, *96*, 3035−3037.

(13) Zhang, Y.; Zhao, D.; Yue, Y. Phase transitions and glass transition in a hyperquenched silica-alumina glass. *J. Am. Ceram. Soc.* **2017**, *100*, 3434−3439.

(14) Kresse, G.; Furthmüller, J. Efficient iterative schemes for ab initio total-energy calculations using a plane-wave basis set. *Phys. Rev. B: Condens. Matter Mater. Phys.* **1996**, *54*, 11169−11186.

(15) Kresse, G.; Joubert, D. From ultrasoft pseudopotentials to the projector augmented-wave method. *Phys. Rev. B: Condens. Matter Mater. Phys.* **1999**, *59*, 1758−1775.

(16) Perdew, J. P.; Burke, K.; Ernzerhof, M. Generalized gradient approximation made simple. *Phys. Rev. Lett.* **1996**, *77*, 3865−3868.

(17) Monkhorst, H. J.; Pack, J. D. Special points for Brillouin-zone integrations. *Phys. Rev. B: Solid State* **1976**, *13*, 5188−5192.

(18) Park, C. H.; Zhang, S.; Wei, S. Origin of p-type doping difficulty in ZnO: The impurity perspective. *Phys. Rev. B: Condens. Matter Mater. Phys.* **2002**, *66*, 073202.

(19) Zhang, S.; Wei, S.; Zunger, A. Intrinsic n-type versus p-type doping asymmetry and the defect physics of ZnO. *Phys. Rev. B: Condens. Matter Mater. Phys.* **2001**, *63*, 75205.

(20) Mattila, T.; Zunger, A. Deep electronic gap levels induced by isovalent P and As impurities in GaN. *Phys. Rev. B: Condens. Matter Mater. Phys.* **1998**, *58*, 1367−1373.

DOI: 10.1021/acs.jpcc.9b09195
J. Phys. Chem. C 2019, 123, 29343−29352

(21) Stupakiewicz, A.; Szerenos, K.; Afanasiev, D.; Kirilyuk, A.; Kimel, A. V. Ultrafast nonthermal photo-magnetic recording in a transparent medium. *Nature* **2017**, *542*, 71−74.
(22) Zhou, Y.; Sun, S.; Song, J.; Xi, S.; Chen, B.; Du, Y.; Fisher, A. C.; Cheng, F.; Wang, X.; Zhang, H.; et al. Enlarged CoO Covalency in Octahedral Sites Leading to Highly Efficient Spinel Oxides for Oxygen Evolution Reaction. *Adv. Mater.* **2018**, *30*, 1802912.
(23) Radovanovic, P. V.; Gamelin, D. R. Electronic absorption spectroscopy of cobalt ions in diluted magnetic semiconductor quantum dots: demonstration of an isocrystalline core/shell synthetic method. *J. Am. Chem. Soc.* **2001**, *123*, 12207−12214.
(24) Manaa, H.; Guyot, Y.; Moncorge, R. Spectroscopic and tunable laser properties of Co^{2+}-doped single crystals. *Phys. Rev. B: Condens. Matter Mater. Phys.* **1993**, *48*, 3633−3645.
(25) Tanabe, Y.; Sugano, S. On the Absorption Spectra of Complex Ions. I. *J. Phys. Soc. Jpn.* **1954**, *9*, 753−766.
(26) Jackson, S. D. Towards high-power mid-infrared emission from a fibre laser. *Nat. Photonics* **2012**, *6*, 423−431.
(27) Gao, G.; Peng, M.; Wondraczek, L. Temperature dependence and quantum efficiency of ultrabroad NIR photoluminescence from Ni^{2+} centers in nanocrystalline Ba-Al titanate glass ceramics. *Opt. Lett.* **2012**, *37*, 1166−1168.
(28) Gelija, D.; Borelli, D. P. R. Effect of concentration variation on 2.0 μm emission of Ho^{3+}-doped SiO_2-Al_2O_3-Na_2CO_3-SrF_2-CaF_2 oxyfluorosilicate glasses. *Appl. Phys. A* **2018**, *124*, 131.
(29) Albers, P.; Stark, E.; Huber, G. Continuous-wave laser operation and quantum efficiency of titanium-doped sapphire. *J. Opt. Soc. Am. B* **1986**, *3*, 134−139.
(30) Fermann, M. E.; Hartl, I. Ultrafast fibre lasers. *Nat. Photonics* **2013**, *7*, 868−874.
(31) Link, S. M.; Maas, D. J. H. C.; Waldburger, D.; Keller, U. Dual-comb spectroscopy of water vapor with a free-running semiconductor disk laser. *Science* **2017**, *356*, 1164−1168.
(32) Guo, H.; Herkommer, C.; Billat, A.; Grassani, D.; Zhang, C.; Pfeiffer, M. H. P.; Weng, W.; Brès, C.-S.; Kippenberg, T. J. Mid-infrared frequency comb via coherent dispersive wave generation in silicon nitride nanophotonic waveguides. *Nat. Photonics* **2018**, *12*, 330−335.
(33) Chen, Y.; Zhao, C.; Chen, S.; Du, J.; Tang, P.; Jiang, G.; Zhang, H.; Wen, S.; Tang, D. Large energy, wavelength widely tunable, topological insulator Q-switched erbium-doped fiber laser. *IEEE J. Sel. Top. Quantum Electron.* **2014**, *20*, 315−322.
(34) Johnson-McDaniel, D.; Barrett, C. A.; Sharafi, A.; Salguero, T. T. Nanoscience of an ancient pigment. *J. Am. Chem. Soc.* **2013**, *135*, 1677−1679.
(35) Strickland, K.; Miner, E.; Jia, Q.; Tylus, U.; Ramaswamy, N.; Liang, W.; Sougrati, M. T.; Jaouen, F.; Mukerjee, S. Highly active oxygen reduction non-platinum group metal electrocatalyst without direct metal-nitrogen coordination. *Nat. Commun.* **2015**, *6*, 7343.
(36) Wei, C.; Feng, Z.; Scherer, G. G.; Barber, J.; Shao-Horn, Y.; Xu, Z. J. Cations in octahedral sites: a descriptor for oxygen electrocatalysis on transition-metal spinels. *Adv. Mater.* **2017**, *29*, 1606800.
(37) Shankar, S.; Peters, M. K.; Steinborn, K.; Krahwinkel, B.; Sonnichsen, F. D.; Grote, D.; Sander, W.; Lohmiller, T.; Rudiger, O.; Herges, R. Light-controlled switching of the spin state of iron (III). *Nat. Commun.* **2018**, *9*, 4750.
(38) Kjær, K. S.; Kaul, N.; Prakash, O.; Chabera, P.; Rosemann, N. W.; Honarfar, A.; Gordivska, O.; Fredin, L. A.; Bergquist, K.; Haggstrom, L.; et al. Luminescence and reactivity of a charge-transfer excited iron complex with nanosecond lifetime. *Science* **2019**, *363*, 249−253.

DOI: 10.1021/acs.jpcc.9b09195
J. Phys. Chem. C 2019, 123, 29343−29352